



# Plastic deformation experiments to high strain on mantle transition zone minerals wadsleyite and ringwoodite in the rotational Drickamer apparatus

Justin Hustoft<sup>a,\*</sup>, George Amulele<sup>a</sup>, Jun-ichi Ando<sup>b</sup>, Kazuhiko Otsuka<sup>a</sup>, Zhixue Du<sup>a</sup>, Zhicheng Jing<sup>a,1</sup>, Shun-ichiro Karato<sup>a</sup>

<sup>a</sup> Department of Geology and Geophysics, Yale University, New Haven, CT, USA

<sup>b</sup> Department of Earth and Planetary Systems Science, Hiroshima University, Higashihiroshima, Japan

## ARTICLE INFO

### Article history:

Received 18 August 2011

Received in revised form

15 October 2012

Accepted 15 November 2012

Editor: L. Stixrude

### Keywords:

wadsleyite  
ringwoodite  
rheology  
transition zone  
subduction

## ABSTRACT

We report the results of plastic deformation experiments on polycrystalline wadsleyite and ringwoodite performed at 15–23 GPa and 1300–2100 K conducted using the rotational Drickamer apparatus (RDA). Wadsleyite was synthesized from fine-grained ( $\sim 2 \mu\text{m}$ ) San Carlos olivine in a Kawai-type multianvil apparatus; the average grain size of the resulting wadsleyite was  $1.2 \mu\text{m}$ . The initial water content of the undeformed wadsleyite was  $24,000\text{--}26,000 \text{ H}/10^6 \text{ Si}$  but the final water content is variable and less than the initial water content. Ringwoodite was synthesized from wadsleyite in situ in the RDA. Both strain and stress were measured in situ using a synchrotron x-ray facility. Determinations of strains and strain rates were made from x-ray radiographs of the sample, using a Mo foil strain marker in the sample assembly. The state of stress was determined from the observed  $d$ -spacing of multiple lattice planes as a function of azimuth angle. Samples were deformed at various strain rates at around  $10^{-4}\text{--}10^{-5} \text{ s}^{-1}$ . Deformation mechanisms were inferred from the stress exponent and the microstructures. We determined the stress exponent  $n$  for wadsleyite to be  $6 \pm 3$ , suggesting dislocation creep was the dominant deformation mechanism in wadsleyite. At grain sizes of  $\sim 1 \mu\text{m}$ , our samples were still deforming primarily by dislocation creep. However, small dislocation-free grains are also observed suggesting that diffusion creep may operate in some parts of our samples.

© 2012 Published by Elsevier B.V.

## 1. Introduction

The mantle transition zone (MTZ, a layer between 410 km and 660 km depth) is the bottommost region of the upper mantle, just above the lower mantle, and has important influences on mantle convection due to complicated changes in the physical properties of materials caused by a series of phase transformations. High-resolution tomographic images show that subducted slabs are deformed in the MTZ, although the nature of deformation varies from one subduction zone to another (e.g., van der Hilst et al., 1991; Káráson and van der Hilst, 2000; Fukao et al., 2001). Among various physical properties, viscosity is a critical parameter that controls convective patterns as it varies with depth (e.g., Davies, 1995; Bunge et al., 1996, 1997). Viscosity of the mantle is determined by the rheological properties of its constituent minerals. Some previous studies showed that the viscosity of the MTZ will determine whether subducted slabs will penetrate into the

lower mantle or be deflected in the MTZ (Davies, 1995; Bina et al., 2001; Fukao et al., 2001; Karato et al., 2001; Richard et al., 2006). In addition, the degree of energy dissipation by slab deformation is an important factor that might control the rate of mantle convection. Consequently, quantifying the viscosity of the MTZ by determining the rheological properties of transition zone minerals is fundamental in our efforts to understand the evolution of the Earth, patterns of convection in the mantle, and the energy budget of the planet. Therefore, to better understand and model convection of the mantle, knowledge of the quantitative rheological properties of wadsleyite and ringwoodite, the primary components of the MTZ (Ringwood, 1991), is needed.

In this study we use the Rotational Drickamer apparatus (RDA) to conduct deformation experiments under the conditions of the MTZ. The RDA, described by Yamazaki and Karato (2001) and Xu et al. (2005), is capable of reaching the pressure and temperature conditions of the mantle transition zone and subsequently performing deformation experiments to large strains using torsion deformation geometry. Previous experimental studies using the RDA have reported the results of plastic deformation experiments on olivine (Nishihara et al., 2008; Kawazoe et al., 2009) and wadsleyite (Kawazoe et al., 2010) up to  $P \sim 17 \text{ GPa}$  and  $T \sim 2000 \text{ K}$ .

\* Corresponding author. Now at: RESPEC Consulting and Services, Rapid City, SD, USA. Tel.: +1 612 508 6791.

E-mail address: [justin.hustoft@respec.com](mailto:justin.hustoft@respec.com) (J. Hustoft).

<sup>1</sup> Now at: GeoSoilEnviroCARS, University of Chicago, Argonne National Laboratory, Argonne, IL, USA.

The rheological properties of ringwoodite have not been explored in the RDA previously, though the rheological properties of ringwoodite have been investigated by others in some preliminary studies. Karato et al. (1998) performed stress relaxation tests on Fe-rich ringwoodite samples ( $\text{Fe}/(\text{Fe}+\text{Mg})=0.4$ ), rather than a typical mantle value of  $\text{Fe}/(\text{Fe}+\text{Mg})=0.1$ , in a multianvil apparatus at  $P \sim 16$  GPa and  $T=1400\text{--}1600$  K (the larger proportion of Fe altered the ringwoodite stability field, allowing the synthesis of ringwoodite at lower pressures). They inferred two deformation mechanisms from microstructural observations and proposed a preliminary deformation mechanism map. Xu et al. (2003) performed stress relaxation tests on ringwoodite at 20 GPa and 1623 K using a two-stage T-cup. However, results from stress-relaxation tests have limitations in obtaining quantitative results on a flow law at steady-state deformation, and in Karato et al. (1998), there were no constraints on the magnitude of stress, and the stress estimates by Xu et al. (2003) have large

uncertainties caused by the use of x-ray peak broadening to determine stress.

Continued refinement of the sample assembly for the RDA has increased the upper limit of the pressures achievable, while improvements in multi-element detectors installed at synchrotron facilities have increased the resolution of stress estimates in the samples (Weidner et al., 2010). Most critical to our improved stress resolution has been the installation of a ten-element detector, allowing for the collection of energy-dispersive x-ray diffraction (EDXRD) patterns over a half-circle. These recent developments have allowed us to use the RDA to explore the rheological properties of mantle minerals under the entire transition zone conditions (14–23 GPa, 1500–2100 K). Here we report the results of plastic deformation experiments on single-phase wadsleyite, ringwoodite, and mixed phases of wadsleyite and ringwoodite, deformed at pressures up to 23 GPa and 2100 K, with stress resolution of 0.1 GPa.

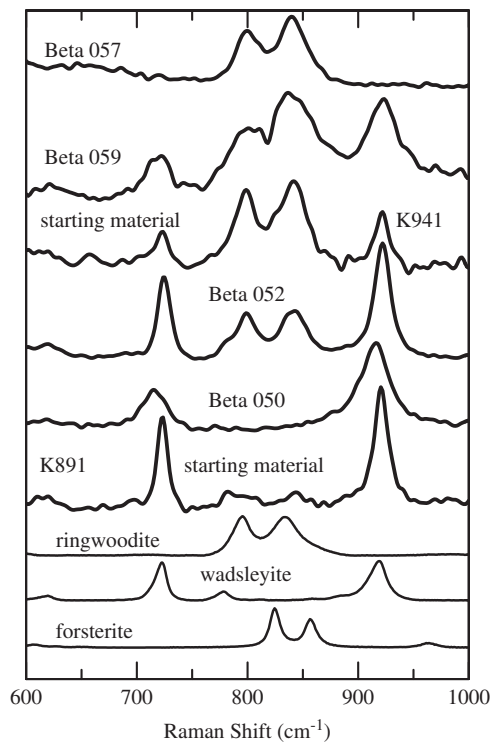


**Fig. 1.** Phases present in the samples were identified using the Raman spectroscopy. The characteristic peaks of wadsleyite ( $721\text{ cm}^{-1}$ ,  $917\text{ cm}^{-1}$ ) and ringwoodite ( $798\text{ cm}^{-1}$ ,  $840\text{ cm}^{-1}$ ) were used to identify the phases present in the starting materials (K891, K941) and the post-deformation samples.

## 2. Experimental methods

### 2.1. Sample preparation

Samples of wadsleyite were synthesized from San Carlos olivine,  $(\text{Mg}_{0.9}\text{Fe}_{0.1})_2\text{SiO}_4$ . The preparation of the olivine powders has been described in detail previously (Kawazoe et al., 2009, 2010); we will provide only a brief overview here. The olivine starting material was ground and filtered to a grain size of less than  $2\text{ }\mu\text{m}$ . The filtered olivine powders were packed in capsules of Ni foil and then loaded into a Kawai-type multianvil press inside a 14/8 assembly. Wadsleyite was synthesized from olivine at 14 GPa and 1300 K. After quenching, the phase of the resulting sample was identified by Raman spectroscopy. The characteristic Raman peaks of wadsleyite ( $721\text{ cm}^{-1}$ ,  $917\text{ cm}^{-1}$ ) and ringwoodite ( $798\text{ cm}^{-1}$ ,  $840\text{ cm}^{-1}$ ), seen in Fig. 1, were used to identify the phases.

Quenched cylinders of wadsleyite were cut into discs  $200\text{ }\mu\text{m}$  thick and then drilled to produce rings with outer diameter 1.6 mm and inner diameter 1.0 mm. The rings of wadsleyite were cut into quarters; two quarter-rings of wadsleyite comprised a single experimental sample with a strain marker of Mo foil between them. The half-ring shape, described in previous publications (Nishihara et al., 2008; Kawazoe et al., 2009, 2010), was selected to minimize gradients in stress and strain across the diameter of the samples.

In a few runs, ringwoodite was formed during the pressurization, and in these cases deformation experiments were conducted in the same run after the synthesis of ringwoodite. Because the microstructures and water content of these starting materials are not well known, the interpretation of the results for ringwoodite has large uncertainties.

**Table 1a**

Experimental conditions and results.

Experiment	Phase	Pressure (GPa)	Temp. (K)	Equivalent strain rate ( $\times 10^{-5}\text{ s}^{-1}$ )	Equivalent strain (%)	Grain size ( $\mu\text{m}$ )		Water content ( $\text{H}/10^6\text{ Si}$ )		Water content (ppm wt% $\text{H}_2\text{O}$ )	
						Initial	Final	Initial	Final	Initial	final
Beta 049	Wadsleyite	15	1300	–	–	1.2	–	24,000	–	0.15	–
Beta 050	Wadsleyite	15	1500	4.9 7.2 17	167	1.2	2–5	24,000	33,000	0.15	0.21
Beta 059	Wads+Ring	18	1900	21	195	–	–	26,000	–	0.17	–
Beta 052	Wads+Ring	18	2100	–	–	1.2	$\sim 1$	24,000	–	0.15	–
Beta 058	Ringwoodite	21	1800	18	156	–	–	26,000	–	0.17	–
Beta 057	Ringwoodite	23	1800	8.0	105	–	0.5–1	26,000	54,000	0.17	0.35

## 2.2. Characterization of samples

Water content and grain size were determined for the starting material and the deformed samples (see Table 1a). Grain sizes were determined from SEM images, such as those seen in Fig. 2, using a linear intercept method, with a correction factor of 1.5 applied to the two-dimensional intercepts to estimate the three-dimensional grain size. Average grain sizes were 1.2  $\mu\text{m}$  for the wadsleyite starting material.

FTIR measurements were carried out at Yale using a Varian FTIR spectrometer with an internal IR source in transmission mode. An unpolarized beam was used with 20–40  $\mu\text{m}$  sized square apertures (depending on the sample size), and 128 or 256 scans used to accumulate individual spectrums. The density factors used in Paterson's calibration were from previously reported results (Kohlstedt et al., 1996).

Representative FTIR spectra of starting materials and recovered samples are shown in Fig. 3, where absorption peaks at 3616, 3581, and 3334  $\text{cm}^{-1}$  are visible. The initial water contents of the starting materials, determined by FTIR spectroscopy, were 24,000–26,000  $\text{H}/10^6$  Si (1500–1600 wt ppm  $\text{H}_2\text{O}$ ) using the calibration of Paterson (1982). The two water contents cited in Table 1a are for two starting materials; K891 for samples Beta 049, 050, and 052, and K941 for samples Beta 057, 058, and 059.

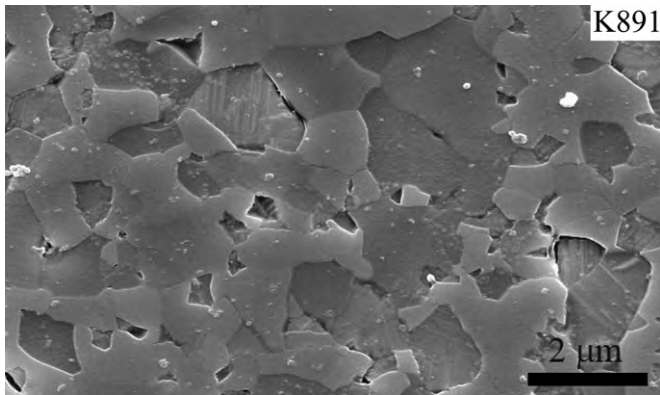


Fig. 2. Secondary electron micrograph of the undeformed, pure wadsleyite starting material for these experiments, synthesized from San Carlos olivine.

## 2.3. Determination of temperature

Temperature was raised by applying direct current across the sample assembly. TiC+diamond disc heaters were used. Temperatures of the samples during annealing and deformation in the RDA were determined after the experiment. A quarter-ring of a mixture of enstatite (opx) and diopside (cpx) was included in all sample assemblies. These opx–cpx mixtures acted as thermometers (Gasparik, 1996). Using the enstatite–diopside thermometer of Gasparik (1996), temperatures were determined by electron microprobe analysis of the recovered pyroxenes. This method of thermometry has been used for previous experiments in the RDA (Nishihara et al., 2008; Kawazoe et al., 2009, 2010). The inclusion of opx–cpx “chips” in the sample assembly allows for post-experiment estimation of temperatures. However, the estimation of temperatures from these opx–cpx interdiffusion couples may be problematic at the conditions of our experiments. Enstatite and diopside are stable up to  $\sim 16$  GPa at  $\sim 1500$   $^{\circ}\text{C}$  (Gasparik, 1996). Beyond these conditions, these minerals transform to garnets or perovskite-structured phases for which the phase diagram is only poorly constrained.

An alternative method for estimating the temperature for samples in the RDA is to use thermocouples to determine power–temperature calibrations. Temperatures in the RDA are measured against power using a thermocouple during separate calibration runs. Inclusion of a thermocouple during experiments is impractical. Using power–temperature calibrations established, we estimated the temperatures as 1300–2100 K (see Table 1a), with uncertainties of  $\pm 200$  K.

## 2.4. X-ray diffraction spectroscopy

Deformation experiments were conducted using the RDA at X17B2 beamline at the National Synchrotron Light Source (NSLS), Brookhaven National Laboratory (BNL). The starting materials were brought to pressure by first raising the load at room temperature. Temperature was then raised by applying direct current across the sample assembly. After annealing for at least 60 min at the target temperature, by which time the differential stress is reduced to  $< 1$  GPa (with the exception of sample Beta 050), constant rotation rate experiments were conducted at rates of  $0.05$ – $0.20^{\circ}/\text{min}$ , resulting in strain rates in the range  $5 \times 10^{-5} \text{ s}^{-1}$ – $2 \times 10^{-4} \text{ s}^{-1}$  (see Table 1a).

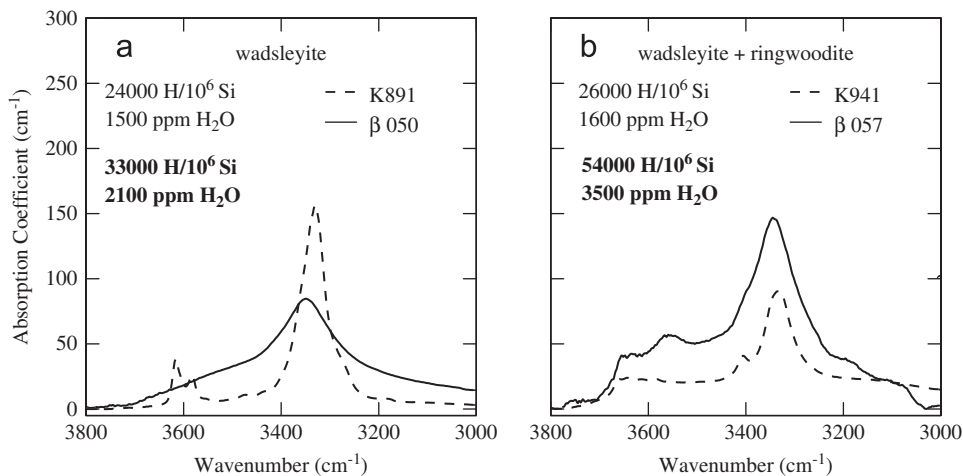
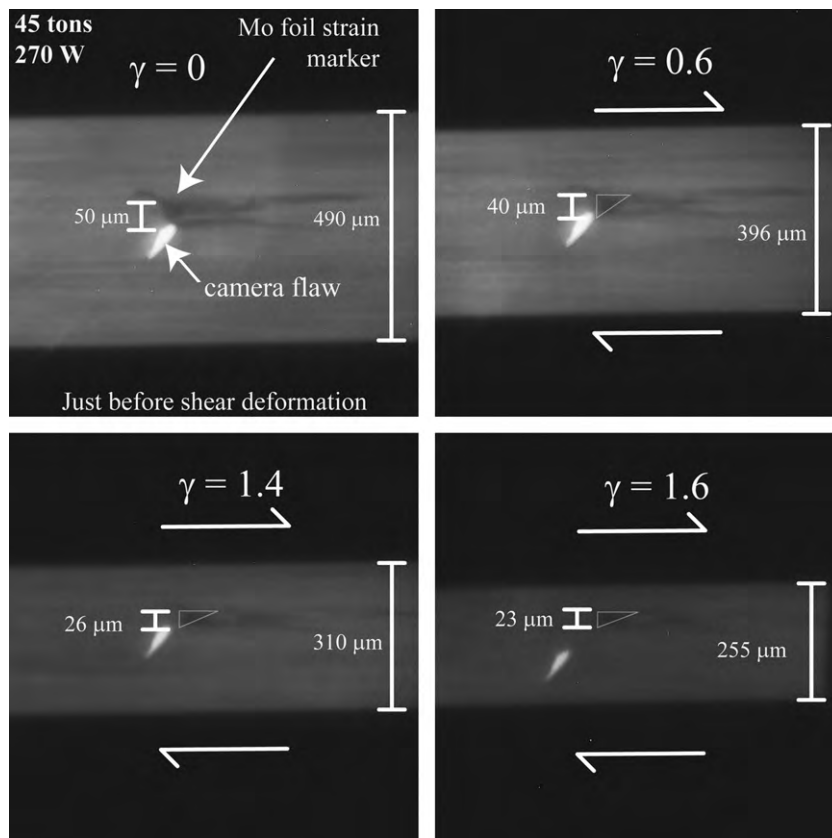


Fig. 3. Unpolarized Fourier transform infrared spectra of starting materials (K891 and K941) and recovered deformed samples. Absorption peaks are noticeable at 3616, 3581, and 3334  $\text{cm}^{-1}$ . Intergranular water may be contributing to the broad band absorption observed in Beta 050.

**Table 1b**  
Equivalent stress values.

Experiment	Wadsleyite equivalent stresses (GPa)						Ringwoodite equivalent stresses (GPa)		
	(040)	(013)	(211)	(141)	(240)	(204)	(311)	(400)	(440)
Beta 049	5.5 ± 1.6	–	–	4.7 ± 0.5	3.0 ± 0.4	3.9 ± 1.1			
Beta 050	5.4 ± 0.6	6.3 ± 1.0	5.9 ± 0.5	4.7 ± 0.3	5.3 ± 0.3	–			
	–	–	–	5.9 ± 0.1	6.1 ± 0.3	–			
	–	–	–	–	6.4	–			
Beta 059	–	–	–	3.4 ± 0.2	3.7 ± 0.1	–			
Beta 052	2.3 ± 0.2	–	–	1.9 ± 0.3	1.9 ± 0.2	–			
Beta 058							1.6 ± 0.1	1.7 ± 0.0	1.7 ± 0.1
Beta 057							2.9 ± 0.1	2.8 ± 0.1	2.8 ± 0.1



**Fig. 4.** Between diffraction exposures, samples are imaged in situ using x-rays. The molybdenum foil strain marker is tracked to record uniaxial and shear strains over the course of experiment. Strain rates are subsequently calculated from the sequence of images. This series of radiographs is from the experiment on sample Beta 050, and highlights both the compression and the simple shear deformation of the sample.

During deformation, deviatoric stress and strain in the samples were measured by in situ x-ray diffraction and radiography, respectively. Energy dispersive x-ray diffraction patterns were collected from 20 to 120 keV. A multi-element detector was used to collect spectra at fixed  $2\theta$  values between 6.607 and 6.730°. The  $2\theta$  values for each element of the detector were calibrated at 0.1 MPa and 300 K, using an alumina standard with known  $d$ -spacings, to a precision of 0.001°.

Strain in samples was monitored in situ by examining the Mo foil strain marker included in the sample assembly. Mo was selected as a strain marker because it is more x-ray opaque and therefore visible in radiographs (see Fig. 4 for an example of the x-radiographs used to determine strain). The Mo foil strain markers were wrapped around the sample to define the top, bottom, and vertical section of the samples for identification in

the radiographs. The horizontal segments of the strain marker allowed determination of compressive displacement while the vertical segment of the strain marker deflected during shear deformation. Uncertainties in strain are from uncertainties in the identification of the edges of the strain marker and the angle of the marker at high strains as a result of thinning of the sample (see Fig. 4), and are typically 25%.

### 3. Experimental results

#### 3.1. Strain and strain rate

An example of the x-radiographs collected to measure strain in the samples during the course of the experiments is depicted in

Fig. 4, where a series of chronological images show the progressive deformation of the strain marker. Strain rates for the samples were determined from these radiographs by fitting the accumulated strain (both uniaxial compression and simple shear) measured from the deflection of the Mo strain marker against time. Equivalent strain for each sample, defined as  $\epsilon_E = \sqrt{\epsilon_U^2 + \frac{4}{3}\epsilon_S^2}$  (Nishihara et al., 2008; Kawazoe et al., 2009) is related to the second invariant of the strain tensor, where  $\epsilon_U$  is uniaxial strain and  $\epsilon_S$  is shear strain. Equivalent strains are plotted against time in Fig. 5. The steady-state strain rate for each sample was determined by fitting the approximately linear increase in equivalent strain after an initial transient. The first two data points are not included in the linear fit of strain versus time for sample Beta 057 because the last data points were at approximately the same stresses, as determined from the XRD data. To determine a steady-state strain rate for the sample Beta 057, the early data points, which may have been experiencing transient stress states during the experiment, were excluded from fitting. Tables 1a and b lists the steady state equivalent strain rates determined in

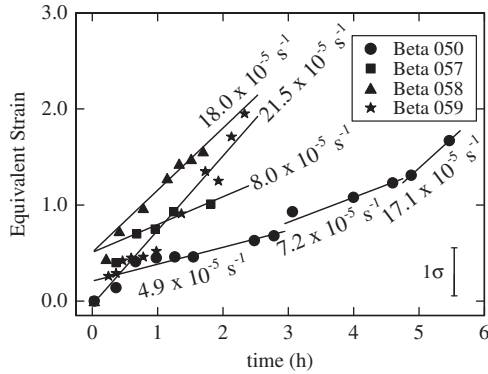


Fig. 5. Equivalent strains, as determined from the uniaxial and shear strains measured in radiographs, plotted against time. The steady-state strain rates are determined by fitting a line to the strain data. The steady-state strain rate for Beta 057 was fit by excluding the first two strain data points, as they are assumed to be in the transient phase of the test. Samples were deformed at constant rotation rates of either 0.05° or 0.10° min<sup>-1</sup>, or in the case of Beta 050, up to 0.20° min<sup>-1</sup>.

Fig. 5. Note that sample Beta 050 was deformed at three different successive rotation rates, 0.05, 0.10, and 0.20° min<sup>-1</sup>, in an effort to constrain the stress exponent *n*.

### 3.2. Determination of stress

Our study has benefited from an improvement in the conical slit system installed at NSLS X17 B2. One benefit has been the higher precision of  $2\theta$ , and another has been the smaller scattering volumes, leading to the increased signal strength from the sample while reducing the interaction with the confining medium. Overall, we have better constraints on the lattice strain ellipse through the increase in the number of detectors, from four in previous runs (e.g., Kawazoe et al., 2010) to ten (Weidner et al., 2010). Uncertainty in stress is limited by the sharpness of the diffraction peaks observed, which constrains the uncertainty of lattice spacing *d*, as well as the number of detectors on the Debye ring that detect the diffraction patterns.

Energy dispersive diffraction patterns were collected at fixed  $2\theta$  values in 900 s exposures during the course of the experiments. An example of the quality of the diffraction patterns collected is shown in Fig. 6. Typically the diffraction peaks from the wadsleyite (240), (141) and (040) planes were the most intense peaks from the sample; other less intense peaks from the sample, such as wadsleyite (112) and the wadsleyite doublet, (013) and (211), were occasionally detectable in some of the diffraction patterns. In the ringwoodite samples, the diffraction peaks from the (311), (400) and (440) planes were the most intense and therefore used to calculate stresses.

Stresses on the samples were determined by fitting the microscopic lattice strains as a function of the azimuth angle (described below). The change in *d*-spacing with azimuth angle  $\Psi$  is highlighted in Fig. 7, where the lattice spacing of the wadsleyite (040), (141) and (240) planes vary sinusoidally with respect to the detectors' azimuth angles. The hydrostatic *d*-spacing  $d_{hkl}^0$ , the uniaxial stress  $\sigma_U$  and the shear stress  $\sigma_S$  felt by the sample were determined by fitting the following equation to the *d*- $\Psi$  data (Xu et al., 2005):

$$d_{hkl} = d_{hkl}^0 \left[ 1 + \frac{\sigma_U}{6G} (1 - 3 \cos^2 \Psi) - \frac{\sigma_S}{2G} \sin \Psi \cos \Psi \right] \quad (1)$$

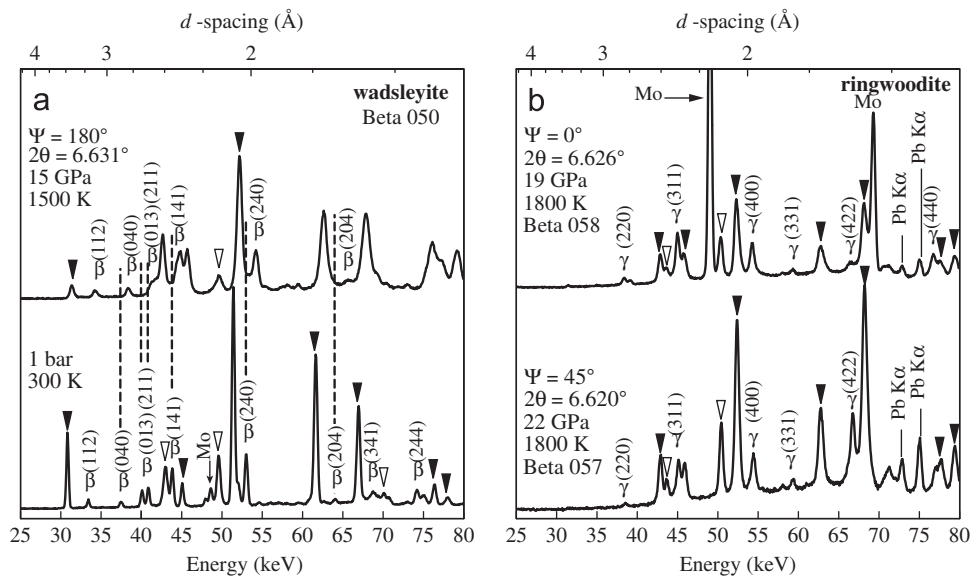
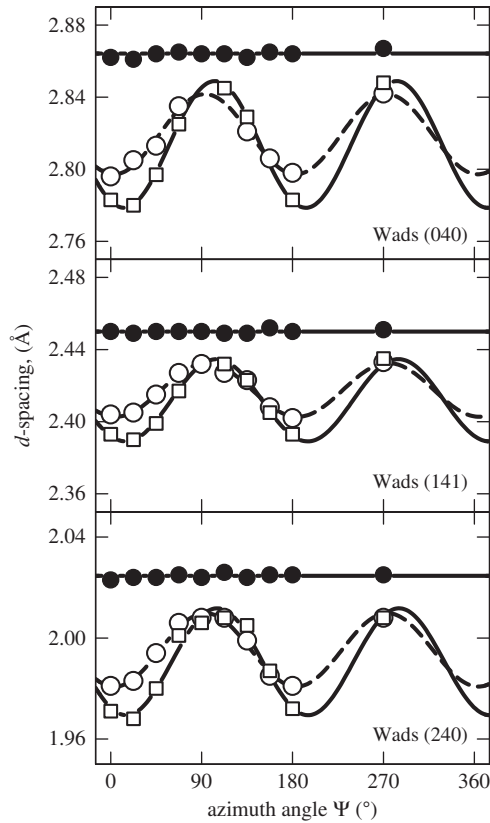


Fig. 6. (a) Energy-dispersive x-ray diffraction (EDXRD) pattern of wadsleyite starting material collected at 1 bar and 300 K. For comparison, above it the EDXRD pattern of wadsleyite at high-*P-T* conditions, just prior to the beginning of shear deformation. (b) EDXRD pattern of ringwoodite (Beta 057) just before shear deformation, and EDXRD pattern of ringwoodite (Beta 058) at high-*P-T* conditions, just prior to the beginning of shear deformation. Filled triangles point to diffraction peaks from alumina and open triangles indicate diffraction peaks from TiC. Wadsleyite and ringwoodite diffraction peaks are labeled by their lattice planes.



**Fig. 7.** Plots of lattice spacing against azimuth angle, for diffraction peaks from wadsleyite (040), (141) and (240) lattice planes. Values for  $d_0$ ,  $\sigma_U$  and  $\sigma_S$  were determined by fitting Eq. (1) to these data. Filled symbols: lattice spacing at room pressure/temperature conditions without any load applied. Open circles: lattice spacing at elevated pressure/temperature conditions prior to deformation ( $\sigma_S=0$ ). Open squares: lattice spacing at experimental conditions, during deformation ( $\sigma_S>0$ ).

where  $G$  is the appropriate elastic modulus for the mineral under investigation. For wadsleyite, a value for the shear modulus  $G_{wads}^0=113$  GPa, was used, with  $G(P,T)$  calculated for the conditions of the experiment using  $\partial G/\partial P=1.5$  and  $\partial G/\partial T=-0.017$  GPa K $^{-1}$  (Li et al., 2001). For ringwoodite the shear modulus at the conditions of the experiments was determined using  $G_{ring}^0=118$  GPa, with  $\partial G/\partial P=1.4$  and  $\partial G/\partial T=-0.0148$  GPa K $^{-1}$  (Mayama et al., 2005). Pressure was calculated from the measured lattice spacings of the sample, using a third-order Birch–Murnaghan equation of state:

$$P = \frac{3}{2}K \left[ \left( \frac{V_0}{V} \right)^{7/3} - \left( \frac{V_0}{V} \right)^{5/3} \right] \left( 1 + \frac{3}{4}(K'-4) \left[ \left( \frac{V_0}{V} \right)^{2/3} - 1 \right] \right) \quad (2)$$

where the unit cell volume  $V$  was determined from the  $d$ -spacings of the various lattice planes. The equivalent stress is defined as  $\sigma_E = \sqrt{\sigma_U^2 + \frac{3}{4}\sigma_S^2}$  (Nishihara et al., 2008; Kawazoe et al., 2009, 2010) (Table 1b). Equivalent stress values determined for each diffraction peak are plotted against accumulated equivalent strain in Fig. 8.

Eq. (1), derived by Singh (1993), assumes that deformation of individual grains in a polycrystalline sample occurs purely elastically including strain accommodation. In addition, in Eq. (1) it is assumed that the relevant elastic constant is the Voigt average of the shear modulus. We adopt this approximation because the elastic model of Singh (1993) is not strictly valid and the influence of plastic deformation to redistribute stress/strain needs to be included in a more complete theory (Karato, 2009). However, in order to apply the theory of Karato (2009) to an orthorhombic

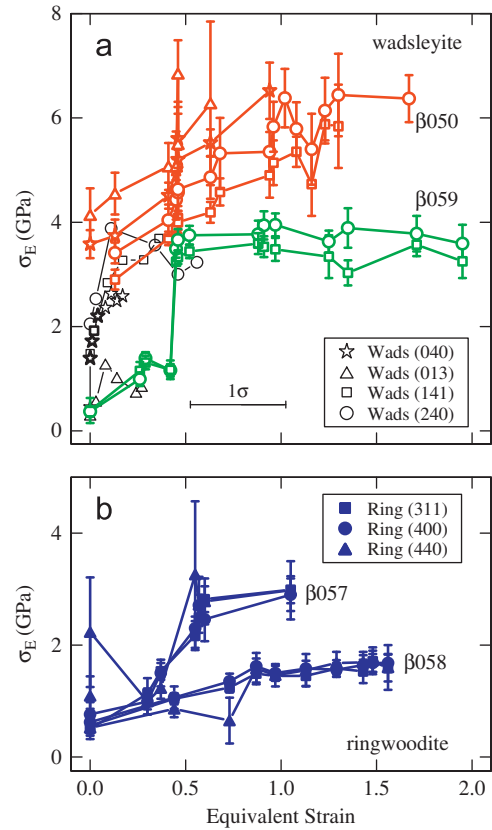


**Fig. 8.** The evolution of equivalent stresses for wadsleyite and ringwoodite with increasing equivalent strain. A steady state value for the equivalent stress is reached by an equivalent strain of approximately 0.50. Data for sample Beta 059 (a mixed phase of ringwoodite and wadsleyite) is determined by assuming the diffraction peaks are from wadsleyite only. Stress–strain data from Nishihara et al. (2008) (open circles and open squares) and Kawazoe et al. (2010) (open triangles and open stars) are plotted for comparison.

crystal, one needs the data on 9 independent diffraction peaks; we use an elastic model by Singh (1993) in this paper.

Steady state equivalent strain rates are plotted against equivalent stresses for various  $(hkl)$  for wadsleyite and ringwoodite in Fig. 9. The results from various lattice planes are plotted individually (samples Beta 049 and 052 are not included because the strain markers were not discernible), rather than averaged to highlight the range of stresses determined from different  $(hkl)$  planes. A fit to the stress for the wadsleyite (240) diffraction peak (the only peak recorded for all three strain rate steps) for Beta 050 at three different equivalent strain rates gives a stress exponent  $n=6 \pm 3$ .

## 4. Discussion

### 4.1. Deformation mechanisms

One of our goals has been to identify the operating deformation mechanisms and determine the flow law for each mechanism for wadsleyite and ringwoodite. To that end, we performed strain-rate stepping experiments to constrain the stress exponent,  $n$ .

The challenge in these strain rate stepping experiments is the identification of a steady-state stress. Once a steady state is judged to have been achieved, the strain rate is changed and the evolution of stress towards a steady state value is observed again. However, one practical difficulty of stepping the strain rate in the RDA is that as strain increases, the thickness of the sample

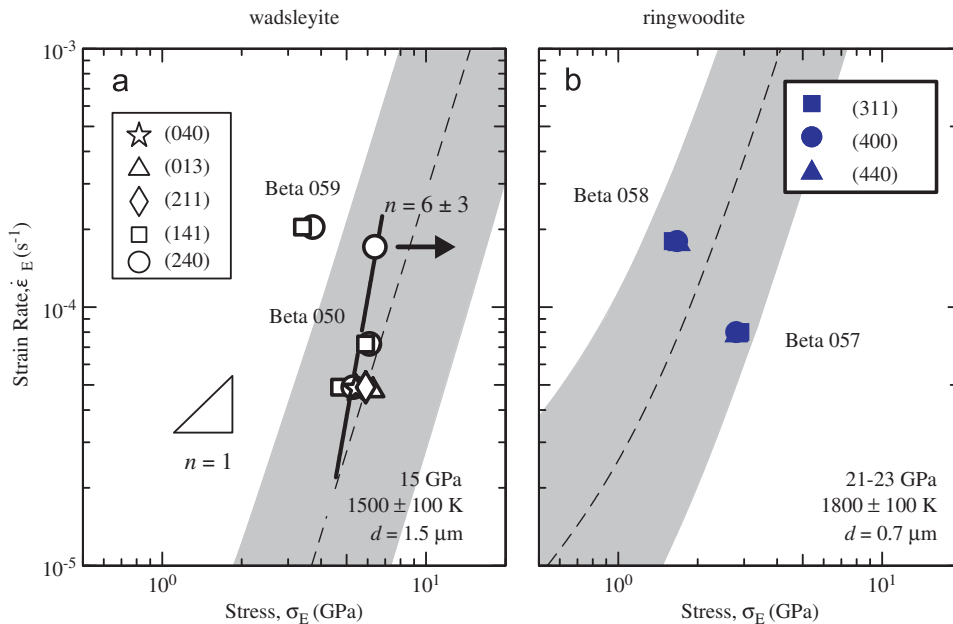


**Fig. 9.** Equivalent strain rates plotted against equivalent stresses for samples of wadsleyite, wadsleyite+ringwoodite, and ringwoodite. (a) One sample in this study (Beta 050) was successfully deformed at three different sequential strain rates. The stress–strain rate data for this sample has a stress exponent  $n = 6 \pm 3$ . (b) Stress and strain rate data for ringwoodite samples compared to the predicted values from Shimojuku et al. (2009). The dashed lines are the strain rates predicted from the model of Shimojuku et al. (2009) with  $n = 3$  at the conditions of these experiments, and the shaded regions are the predicted strain rates with temperature  $\pm 200$  K of the estimated temperature for these experiments.

is reduced; as the sample thins, the tungsten carbide anvils may block detectors on the Debye ring. Thinner samples also lead to smaller interaction volumes and thus reduced intensity of the diffraction peaks, making identification of peaks more difficult. As such, as strain increases, the quality of diffraction patterns begin to degrade, making determination of stresses less precise and the identification of steady state stresses complicated.

Another difficulty in performing these strain rate stepping experiments is the longevity of the furnace. If the furnace fails before a second or third strain rate step can be performed, no constraints on the stress exponent are possible. Our experiment conducted at three strain rate steps for one sample of wadsleyite is therefore a major step for the determination of a stress exponent for a transition zone mineral.

A salient point in this study is the magnitude of the stresses determined by x-ray diffraction. Previous studies using the RDA to perform deformation experiments also reported gigapascal-level stresses in specimens (Nishihara et al., 2008; Kawazoe et al., 2009, 2010). Low temperatures, high pressures and fast strain-rates are the obvious cause for high stress magnitude. Also strain hardening during plastic deformation could cause high stresses as seen in Beta 50.

The slope of the stress–strain rate data for wadsleyite in Fig. 9a,  $n = 6 \pm 3$ , suggests that dislocation creep is the dominant deformation mechanism at our experimental conditions (see Table 1a). As a caveat, we must note that the third strain rate step in experiment Beta 050 was interrupted by the failure of the furnace. The sample may not have reached a steady state stress at that strain rate. The arrow in Fig. 9a indicates that the stress possibly would have evolved to a larger value if the furnace failure had not terminated the test, but the stress is unlikely to have increased significantly enough to suggest that the stress exponent would be below  $n = 3$ . For comparison, a slope of  $n = 1$ , characteristic of diffusion creep, is included.

We prepared ten TEM foils from the recovered samples (two for Beta 050, three for Beta 052 and five for Beta 057) by using a

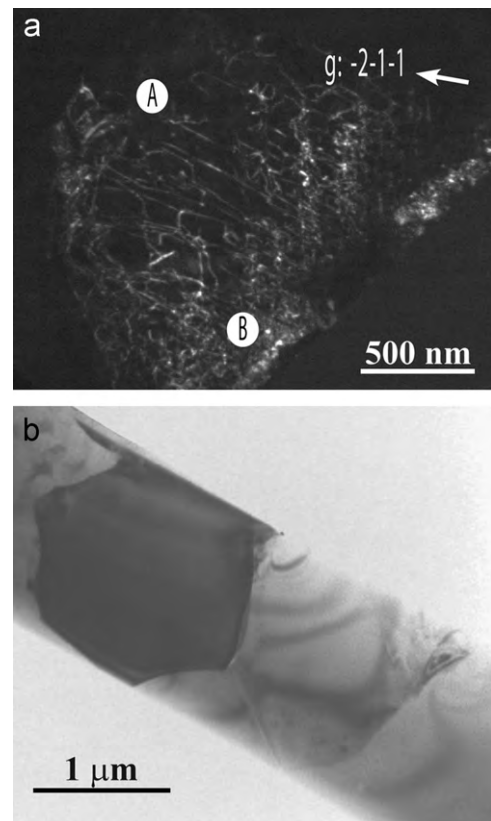


**Fig. 10.** TEM images of the recovered samples. (a) Weak-beam dark-field image ( $g = -2-1-1$ ) of wadsleyite grain observed in Beta 052. The individual dislocations can be seen in the area “A”, while they are not in area “B” due to very high dislocation density (strong tangling) which is showing complex contrast. All grains in Beta 050 and 057 exhibit the same dislocation microstructure in area “B”. (b) Bright field image of microstructure of Beta 052. Most grains in Beta 052 are dislocation free (or very rare) with straight grain boundary.

focused ion beam method (FIB). The typical microstructure of wadsleyite in these samples is tangled dislocations, which imply high stress conditions (Fig. 10a). The tangling developed in Beta 050 is the strongest among these samples. This microstructure should be reflective of the final high strain rate step (ca.  $17 \times 10^{-5} \text{ s}^{-1}$ ) and could be caused by the lower temperature condition (1500 K). Evidence of dislocation recovery (e.g., sub-grain boundaries made by dislocation arrays) was not observed in all TEM samples. Evidence of dislocation recovery (e.g., sub-grain boundaries made by dislocation arrays) was not observed in all TEM samples. This observation may imply that the conditions for deformation are still in the Peierls regime. Indeed, the estimated stress exponent is relatively high ( $\sim 6$ ) in our experiments. However, the smaller grains (ca.  $1 \mu\text{m}$ ) with no dislocation and strain grain boundary are observed in the recovered sample of Beta 052 (Fig. 10b). The presence of these nearly dislocation-free grains suggests the operation of diffusion creep in some regions of the samples. The dislocation-free grains can also be formed during dislocation creep by dynamic recrystallization. However, the recrystallized grain is deformed by on-going dislocation mechanism, which results in production of new dislocations in it. Therefore, the existence of both microstructures such as tangled and absence of dislocations suggests that the deformation conditions of these samples are close to the boundary between dislocation and diffusion creep.

Creep rates of minerals can be estimated by assuming that the slowest diffusing species controls the creep rate. Shimojuku et al. (2009) conducted self-diffusion experiments on wadsleyite and ringwoodite under  $P$ - $T$  conditions similar to those of our experiments. They concluded that Si is the slowest diffusing species of the major elements in wadsleyite and ringwoodite. The authors then constructed deformation mechanism maps for wadsleyite and ringwoodite based on their measurements of Si and O self-diffusion rates in these minerals using a dislocation creep model by Weertman (1999) and the Nabarro–Herring model of diffusion creep. Their models for rheological behavior are plotted in Fig. 9a and b for comparison with our data.

The strain rates for dislocation creep in wadsleyite determined from the parameters of Shimojuku et al. (2009) using the model of Weertman (1999) for dislocation creep are plotted in Fig. 9 for the conditions of our experiments. Such an exercise has large uncertainties because models for dislocation creep are not well established. For instance, the model of Weertman (1999) does not include the influence of jog concentration and it has a free adjustable parameter  $l_g/l_c$ , the glide-to-climb ratio (we show results for  $l_g/l_c = 1$ ). Furthermore, using a stress exponent of  $n = 6$  as determined from our data in the model of Shimojuku et al. (2009) would not account for our data at all. Consequently, a comparison of our data with Shimojuku et al. (2009) is only for illustrative purposes. The ringwoodite data from this study and the predicted dislocation creep strain rates for ringwoodite agree reasonably well, possibly due to the large uncertainties in experimental conditions.

#### 4.2. Water contents

Controlling water content in the RDA is difficult. Encapsulating the sample to retain water would obscure the sample to x-rays. Annealing the sample prior to deformation usually leads to loss of water; the water content of the recovered sample is assumed to be the water content during the experiment. Samples can also absorb water from the pressure medium, in this case, pyrophyllite. Intergranular water contributed from the pyrophyllite gasket may be responsible for the broad absorption band observed in Beta 050, as seen in Fig. 3. However, the flux of water into and out of the specimens is unknown during the actual experiment.

The water contents of our starting materials, 24,000–26,000 H/10<sup>6</sup> Si, are comparable to the initial water contents for samples described in Kawazoe et al. (2010) (32,000–36,000 H/10<sup>6</sup> Si). However, the water contents of our recovered deformed samples are much greater than those of Kawazoe et al. (2010), though much less than those of Jacobsen et al. (2005) or Demouchy et al. (2011) by at least 4 orders of magnitude. Whereas the recovered wadsleyite samples of Kawazoe et al. (2010) had water contents of  $< 2200 \text{ H}/10^6 \text{ Si}$ , and samples of wadsleyite characterized by Jacobsen et al. (2005) had water contents of 3200 to 6000 ppm wt H<sub>2</sub>O ( $5\text{--}9 \times 10^{10} \text{ H}/10^6 \text{ Si}$ ) samples in this study had contents of 33,000–54,000 H/10<sup>6</sup> Si. Compared at the same strain-rate and temperature, our wadsleyite sample with higher water content has somewhat smaller stress, approximately 1/3 the equivalent stress of the samples described by Kawazoe et al. (2010). This reduction in stress could be attributed to a water weakening effect, but is more likely a result of the confluence of uncertainties in the conditions at which these experiments were run. The large uncertainties in temperature and deformation mechanism make the quantitative discussion of water effect difficult.

#### 4.3. Implications

Grain size reduction during phase transformation can lead to rheological weakening, if the grain size remains small (Riedel and Karato, 1997; Karato et al., 2001), allowing the material to deform by grain-size sensitive creep. Our experiments establish that, for laboratory conditions ( $10^{-5} \text{ s}^{-1}$ ), the minimum grain size for diffusion creep to dominate must be smaller than  $1 \mu\text{m}$ . Using a scaling law with a stress exponent  $n = 3$  and assuming a grain size exponent  $m = 2$ , at mantle conditions ( $10^{-15} \text{ s}^{-1}$ ), the grain size of wadsleyite must be smaller than 3 mm, and for ringwoodite 2 mm, for these minerals to deform dominantly by diffusion creep.

### 5. Conclusions

In this study, we have conducted quantitative in situ rheological measurements up to  $P = 23 \text{ GPa}$  and  $T = 2100 \text{ K}$  using the RDA. While wadsleyite has been deformed in the RDA before (see Kawazoe et al., 2010), this new data benefited from additional detectors installed at the BNL NSLS X17B2 (see Weidner et al., 2010), resulting in higher resolution of stresses, and some constraints on the flow law were obtained.

Combined with the microstructural observations by TEM and a comparison with creep models, we conclude that the deformation conditions in our experiments are close to the boundary between dislocation creep and diffusion creep. A preliminary estimate of this boundary was made and the results suggest that diffusion creep will dominate if grain-size is reduced below 2 mm (at a geological strain rate of  $10^{-15} \text{ s}^{-1}$ ). Such a mechanism transition will lead to rheological weakening which plays an important role in slab deformation (Karato et al., 2001).

We have also obtained the first data suggesting the weakening effects of water. A recent study on electrical conductivity (e.g., Karato, 2011) suggests a high but variable water content in the mantle transition zone (MTZ). This implies that the rheological properties of the MTZ will change regionally due to the variation in water content as well as due to the variation in temperature.

We have demonstrated the capability of reaching pressures as high as 23 GPa in the RDA, allowing rheological properties measurements of nearly the entire upper mantle. Further studies with controlled water contents, over a wider range of  $P$ - $T$  conditions, will allow us to measure values of the activation energy and activation volumes for wadsleyite and ringwoodite. Further improvements in

the pressure-generating capability of the RDA will allow the investigation of the rheological properties of the lower mantle.

## Acknowledgments

We thank Michael Vaughan, Liping Wang, and Donald Weidner for technical assistance at NSLS. William Durham is thanked for discussions on the analysis of x-ray observations. This work was supported by NSF and COMPRES and a Bateman fellowship at Yale to JH.

## References

- Bina, C.R., Stein, S., Marton, F.C., Van Ark, E.M., 2001. Implications of slab mineralogy for subduction dynamics. *Phys. Earth Planet. Inter.* 127, 51–66.
- Bunge, H.-P., Richards, M.A., Baumgardner, J.R., 1996. Effect of depth-dependent viscosity on the planform of mantle convection. *Nature* 379, 436–438.
- Bunge, H.-P., Richards, M.A., Baumgardner, J.R., 1997. A sensitivity study of three-dimensional spherical mantle convection at  $10^9$  Rayleigh number: effects of depth-dependent viscosity, heating mode, and an endothermic phase change. *J. Geophys. Res.* 102 (B6), 11991–12007.
- Davies, G.F., 1995. Penetration of plates and plumes through the mantle transition zone. *Earth Planet. Sci. Lett.* 133, 507–516.
- Demouchy, S., Mainprice, D., Tommasi, A., Couvy, H., Barou, F., Frost, D.J., Cordier, P., 2011. Forsterite to wadsleyite phase transformation under shear stress and consequences for the Earth's mantle transition zone. *Phys. Earth Planet. Inter.* 184, 91–104.
- Fukao, Y., Widiyantoro, S., Obayashi, M., 2001. Stagnant slabs in the upper and lower mantle transition region. *Rev. Geophys.* 39, 291–323.
- Gasparik, T., 1996. Melting experiments on the enstatite-diopside join at 70–224 kbar, including the melting of diopside. *Contrib. Mineral. Petrol.* 124, 139–153.
- Jacobsen, S.D., Demouchy, S., Frost, D.J., Boffa-Ballaran, T., 2005. A systematic study of OH in hydrous wadsleyite from polarized infrared spectroscopy and single crystal X-ray diffraction: oxygen sites for hydrogen storage in Earth's interior. *Am. Mineral.* 90, 61–70.
- Kárason, H., van der Hilst, R.D., 2000. Constraints on mantle convection from seismic tomography. In: Richards, M.R., Gordon, R., van der Hilst, R.D. (Eds.), *The History and Dynamics of Global Plate Motion*, Geophysical Monograph, vol. 121. American Geophysical Union, Washington, DC, pp. 277–288.
- Karato, S., 2009. Theory of lattice strain in a material undergoing plastic deformation: basic formulation and applications to a cubic crystal. *Phys. Rev. B* 79, 214106.
- Karato, S., 2011. Water distribution across the mantle transition zone and its implications for global material circulation. *Earth Planet. Sci. Lett.* 301, 413–423.
- Karato, S., Dupas-Bruzek, C., Rubie, D.C., 1998. Plastic deformation of silicate spinel under the transition-zone conditions of the Earth's mantle. *Nature* 395, 266–269.
- Karato, S., Reidel, M.R., Yuen, D.A., 2001. Rheological structure and deformation of subducted slabs in the mantle transition zone: implications for mantle circulation and deep earthquakes. *Phys. Earth Planet. Inter.* 127, 83–108.
- Kawazoe, T., Karato, S., Otsuka, K., Jing, Z., Mookherjee, M., 2009. Shear deformation of dry polycrystalline olivine under deep upper mantle conditions using a rotational Drickamer apparatus (RDA). *Phys. Earth Planet. Inter.* 174, 128–137.
- Kawazoe, T., Karato, S., Ando, J., Jing, Z., Otsuka, K., Hustoft, J.W., 2010. Shear deformation of polycrystalline wadsleyite up to 2100 K at 14–17 GPa using a rotational Drickamer apparatus (RDA). *J. Geophys. Res.* 115, B08208, <http://dx.doi.org/10.1029/2009JB007096>.
- Kohlstedt, D.L., Keppler, H., Rubie, D.C., 1996. Solubility of water in the alpha, beta, and gamma phases of  $(\text{Mg,Fe})_2\text{SiO}_4$ . *Contrib. Mineral. Petrol.* 123, 345–357.
- Li, B., Liebermann, R., Weidner, D.J., 2001.  $P$ - $V_p$ - $V_s$ - $T$  measurements on wadsleyite to 7 GPa and 873 K: Implications for the 410-km seismic discontinuity. *J. Geophys. Res.* 106 (B12), 30575–30591.
- Mayama, N., Suzuki, I., Saito, T., Ohno, I., Katsura, T., Yoneda, A., 2005. Temperature dependence of the elastic moduli of ringwoodite. *Phys. Earth Planet. Inter.* 148, 353–359.
- Nishihara, Y., Tinker, D., Kawazoe, T., Xu, Y., Jing, Z., Matsukage, K., Karato, S., 2008. Plastic deformation of wadsleyite and olivine at high-pressure and high-temperature using a rotational Drickamer apparatus (RDA). *Phys. Earth Planet. Inter.* 170, 156–169.
- Paterson, M.S., 1982. The determination of hydroxyl by infrared absorption in quartz, silicate glasses and similar materials. *Bull. Mineral.* 105, 20–29.
- Richard, G., Bercovici, D., Karato, S., 2006. Slab dehydration in the Earth's mantle transition zone. *Earth Planet. Sci. Lett.* 251, 156–167.
- Riedel, M.R., Karato, S., 1997. Grain-size evolution in subducted oceanic lithosphere associated with the olivine-spinel transformation and its effects on rheology. *Earth Planet. Sci. Lett.* 148, 27–43.
- Ringwood, A.E., 1991. Phase transformations and their bearing on the constitution and dynamics of the mantle. *Geochim. Cosmochim. Acta* 55, 2083–2110.
- Shimozuku, A., Kubo, T., Ohtani, E., Nakamura, T., Okazaki, R., Dohmen, R., Chakraborty, S., 2009. Si and O diffusion in  $(\text{Mg,Fe})_2\text{SiO}_4$  wadsleyite and ringwoodite and its implications for the rheology of the mantle transition zone. *Earth Planet. Sci. Lett.* 284, 103–112.
- Singh, A.K., 1993. The lattice strains in a specimen (cubic system) compressed nonhydrostatically in an opposed anvil device. *J. Appl. Phys.* 73 (9), 4278–4286.
- van der Hilst, R., Engdahl, R., Spakman, W., Nolet, G., 1991. Tomographic imaging of subducted lithosphere below northwest Pacific island arcs. *Nature* 353, 37–43.
- Weertman, J., 1999. Microstructural mechanisms of creep. In: Meyers, M.A., Armstrong, R.W., Kirschner, H. (Eds.), *Mechanics and Materials: Fundamentals and Linkages*. John Wiley and Sons, pp. 451–488.
- Weidner, D., Vaughan, M.T., Wang, L., Long, H., Li, L., Dixon, N.A., Durham, W.B., 2010. Precise stress measurements with white synchrotron x-rays. *Rev. Sci. Instrum.* 81, 013903.
- Xu, Y., Weidner, D.J., Chen, J., Vaughan, M.T., Wang, Y., Uchida, T., 2003. Flow-law for ringwoodite at subduction zone conditions. *Phys. Earth Planet. Inter.* 136, 3–9.
- Xu, Y., Nishihara, Y., Karato, S., 2005. Development of a rotational Drickamer apparatus for large-strain deformation experiments at deep Earth conditions. In: Chen, J., Wang, Y., Duffy, T.S., Shen, G., Dobrzynetskaia, L.F. (Eds.), *Advances in High-Pressure Technology for Geophysical Applications*. Elsevier, pp. 167–182.
- Yamazaki, D., Karato, S., 2001. High-pressure rotational deformation apparatus to 15 GPa. *Rev. Sci. Instrum.* 72 (11), 4207–4211.